

Global gray and white matter metabolic changes after simian immunodeficiency virus infection in CD8-depleted rhesus macaques: proton MRS imaging at 3 T

William E. Wu^a, Assaf Tal^a, Ivan I. Kirov^a, Henry Rusinek^a, Daniel Charytonowicz^a, James S. Babb^a, Eva-Maria Ratai^b, R. Gilberto Gonzalez^b and Oded Gonen^{a*}

To test the hypotheses that global decreased neuro-axonal integrity reflected by decreased *N*-acetylaspartate (NAA) and increased glial activation reflected by an elevation in its marker, the *myo*-inositol (*ml*), present in a CD8-depleted rhesus macaque model of HIV-associated neurocognitive disorders. To this end, we performed quantitative MRI and $16 \times 16 \times 4$ multivoxel proton MRS imaging (TE/TR = 33/1400 ms) in five macaques pre- and 4–6 weeks post-simian immunodeficiency virus infection. Absolute NAA, creatine, choline (Cho), and *ml* concentrations, gray and white matter (GM and WM) and cerebrospinal fluid fractions were obtained. Global GM and WM concentrations were estimated from 224 voxels (at 0.125 cm^3 spatial resolution over ~35% of the brain) using linear regression. Pre- to post-infection global WM NAA declined 8%: 6.6 ± 0.4 to $6.0 \pm 0.5 \text{ mM}$ ($p = 0.05$); GM Cho declined 20%: 1.3 ± 0.2 to $1.0 \pm 0.1 \text{ mM}$ ($p < 0.003$); global *ml* increased 11%: 5.7 ± 0.4 to $6.5 \pm 0.5 \text{ mM}$ ($p < 0.03$). Global GM and WM brain volume fraction changes were statistically insignificant. These metabolic changes are consistent with global WM (axonal) injury and glial activation, and suggest a possible GM host immune response. Copyright © 2013 John Wiley & Sons, Ltd.

Keywords: animal disease models; brain; HIV-1; *Macaca mulatta*; MRS; simian immunodeficiency virus

INTRODUCTION

HIV-associated neurocognitive disorders (HAND) are a significant problem for the million infected in the US alone (1,2). Unfortunately, incomplete understanding of its pathogenesis hinders development of effective therapies. Recent evidence has shown that in spite of the benefits of highly-active antiretroviral therapy, incidence of HAND among advanced HIV patients has not changed and its prevalence continues to climb (3). Moreover, mounting evidence (4,5) suggests that even when maximally suppressed in cerebrospinal fluid (CSF) and blood plasma, HIV may still facilitate dementia. This is thought to be due to patients living significantly (up to 20+ years) longer with the disease (6), allowing infected monocytes, macrophages and microglia to produce a toxic cascade that ultimately results in neuronal death (7). MRI and proton-MRS (^1H -MRS) have been useful in detecting brain abnormalities (8–11), and provide critical knowledge of the dynamics of cerebral injury during HIV-infection (12–15).

Due to practical challenges commonly associated with retrospective HIV studies, e.g., unknown infection date and overlapping secondary conditions, animal models are often used (16). Simian immunodeficiency virus (SIV)-infected rhesus macaque shares a similar pathology with HIV-infection, including the development of AIDS, disease of the central nervous system and cognitive and/or behavioral deficits (17–20). Although several ^1H -MRS studies of SIV-infected macaque models are reported, they all used low spatial resolution ($>3 \text{ cm}^3$) single voxels in

few brain regions that typically suffer CSF, gray and white matter (GM and WM) partial volume (21–23). Consequently, one outstanding, therapy-relevant question remains: the relative dysfunction of the global GM versus WM.

Indeed, prior histopathology of SIV-infected macaques has shown neuro-axonal dysfunction and death in both GM and WM regions (24,25), as well as glial activation in subcortical WM and cortical GM suggestive of developing encephalitis (26,27). Based on these findings, the aim of this study was to test the hypothesis that decreases in global GM and WM *N*-acetylaspartate (NAA), the marker for neuronal integrity, and elevated global GM and WM

* Correspondence to: Oded Gonen, Department of Radiology, New York University School of Medicine, 660 First Avenue, 4th Floor, New York, New York 10016, USA. E-mail: oded.gonen@med.nyu.edu

a W. E. Wu, A. Tal, I. I. Kirov, H. Rusinek, D. Charytonowicz, J. S. Babb, O. Gonen Department of Radiology, New York University School of Medicine, New York, NY, 10016, USA

b E.-M. Ratai, R. Gilberto Gonzalez Massachusetts General Hospital, Athinoula A. Martinos Center for Biomedical Imaging and Neuroradiology Division, Charlestown, MA, 02129, USA

Abbreviations used: AP, anterior-posterior; CD8, cluster of differentiation 8; Cho, choline; Cr, creatine; CRLBs, Cramer–Rao lower bounds; CSF, cerebrospinal fluid; FWHM, full-width at half-maximum; GM, gray matter; HAND, HIV-associated neurocognitive disorders; HIV, human immunodeficiency virus; IS, inferior-superior; LR, left-right; *ml*, *myo*-inositol; NAA, *N*-acetylaspartate; SIV, Simian immunodeficiency virus; TSE, turbo spin echo; VOI, volume-of-interest; WM, white matter.

myo-inositol (*ml*), the marker for glial activation (28,29), are already detectable in an accelerated non-human primate model of HAND. To overcome the spatial coverage restriction of single voxel ^1H -MRS, we used an approach that combines the data from high-, 0.125 cm^3 , spatial resolution 3D multivoxel ^1H -MRS imaging with MRI tissue segmentation (30), to analyze hundreds of voxels cooperatively, thereby increasing the overall precision (30) – at the cost of sensitivity to possible regional variations. We use this approach to compare the global GM and WM levels of NAA, *ml*, creatine (Cr) and choline (Cho) – the markers of cellular energy/density and membrane turnover (28,29) – in a large, 28 cm^3 (~35%) portion of five rhesus macaque brains before and 4–6 weeks after SIV infection, when they are persistently CD8+ lymphocyte-depleted (23).

MATERIALS AND METHODS

Non-human primates

Five (two females and three males; 5.0–8.6 kg weight) healthy 3- to 4-year-old adult rhesus macaques (*Macaca mulatta*) were scanned under constant veterinary supervision. Each was tranquilized with 15–20 mg/kg intramuscular ketamine hydrochloride and intubated to ensure a patent airway during the experiment (no mechanical ventilation was needed). Intravenous injection of 0.4 mg/kg atropine was used to prevent bradycardia. A continuous infusion of 0.25 mg/kg/minute propofol was maintained via a catheter in a saphenous vein. Heart and respiratory rates, oxygen saturation and end-tidal CO_2 were monitored continuously and a water blanket was used to prevent hypothermia. All animals were then subsequently infected by intravenous injection with SIV and their CD8+ lymphocytes persistently depleted (>28 days post-infection) to speed up progression to AIDS and SIV encephalitis, [both late-stage events similar to those of HIV-infection (31,32)] with an antibody targeted against CD8 (cM-T807) at 6, 8 and 12 days post-inoculation. CD8+ depletion without SIV-infection has been demonstrated not to produce metabolic changes or pathological abnormalities in the rhesus macaque brain (33). The animals were rescanned 4 or 6 weeks later to assess disease activity. The protocol was approved by the Harvard Medical School and Massachusetts General Hospital Institutional Animal Care and Utilization Committees.

MRI

All experiments were done in a 3 T whole-body MR imager (Magnetom TIM Trio, Siemens AG, Erlangen, Germany), running software version VB13P. It was equipped with the manufacturer's circularly-polarized transmit-receive knee-coil capable of delivering a peak 2 kHz (45.2 μT) radio-frequency (RF) \mathbf{B}_1 field with ~1 kW of power. To guide the ^1H -MRS volume-of-interest (VOI) and for tissue segmentation, sagittal and axial T2-weighted turbo spin echo (TSE) MRI: TE/TR = 16/7430 ms, $140 \times 140\text{ mm}^2$ field-of-view (FOV), 512×512 matrix, were acquired. To cover the entire macaque head, 24 sagittal images 2.0 mm thick each and 40 axial images 1.2 mm thick each were obtained, as shown in Fig. 1.

Multivoxel 3D ^1H -MRS imaging

A 4.0 cm anterior-posterior (AP) \times 3.5 cm left-right (LR) \times 2.0 cm inferior-superior (IS) = 28 cm^3 VOI was image-guided onto the corpus callosum and angled along the genu-splenium line of each animal to maximize the number of brain voxels within it

while avoiding air-filled sinuses and skull lipids, as shown in Fig. 1. The manufacturer's automatic procedure adjusted the first- and second-order shims to $26 \pm 1\text{ Hz}$ full-width-at-half-maximum (FWHM) VOI water line. The VOI was excited using TE = 33 ms PRESS with two, 1-cm-thick, second-order Hadamard-encoded slabs (two slices 0.5 cm thick each), interleaved along the IS direction every 720 ms for an effective TR of 1440 ms for each slab (and slice), as shown in Fig. 1b. This results in an optimal signal-to-noise ratio (SNR) and spatial coverage (34), as well as allows a strong, 9 mT/m Hadamard slice-selection gradient to keep the maximal 1.6 ppm chemical shift displacement between NAA and *ml* to 0.5 mm, 10% of each slice's thickness (35). The four slices' planes were encoded with 16×16 2D-chemical shift imaging over an $8 \times 8\text{ cm}^2$ (LR \times AP) FOV to yield nominal $(0.5\text{ cm})^3 = 0.125\text{ cm}^3$ voxels [$1.12 \times 1.12 \times 0.75 \approx 0.15\text{ cm}^3$ given the FWHM of the 2D point spread function (36)]. The VOI was defined in their planes by the two 9 ms, 4.9 kHz bandwidth 180° RF pulses, under 3.3 and 2.9 mT/m. The localization grid produced 8×7 voxels per slice, for a total of 224 in the VOI, as shown in Fig. 1. The MRS signal was acquired for 256 ms at $\pm 1\text{ kHz}$ bandwidth. Each $16 \times 16 \times 2$ ^1H -MRS imaging scan took ~12.5 min and for 4 averages ~50 min.

Brain volumetry

The TSE images were segmented with our FireVoxel package (37). It first corrects all images for non-uniform intensities owing to the coil's RF inhomogeneities, using the common histogram devolution technique of Sled *et al.* (38). Next, a WM signal intensity, I_{WM} , is selected in a periventricular 'seed' region. After automatic detection of all pixels at or above 50% (but below 172.5% to exclude CSF) of I_{WM} , a tissue-mask is constructed per slice in three steps: morphological erosion, recursive region growth retaining pixels connected to the seed and morphological inflation to reverse the effect of erosion. Pixels of intensity above 172.5% of I_{WM} as CSF, as shown in Fig. 2a. Following a similar process, the program classifies all pixels above 120% (but below 172.5%) of I_{WM} , as part of the GM mask; and pixels under 120% (but over 50% to exclude air cavities) as WM, as shown in Fig. 2b and c. The masks were co-registered with the ^1H -MRS imaging grid using in-house software (MATLAB, The Mathworks Inc., Natick, MA, USA), which estimated their volumes in every j -th voxel in the k -th animal (V_{jk}^{GM} , V_{jk}^{WM} and V_{jk}^{CSF}).

Metabolic quantification

The ^1H -MRS imaging data were processed offline using in-house software written in IDL (Research Systems Inc., Boulder, CO, USA). The data were voxel-shifted to align the NAA grid with the VOI, then Fourier transformed in the time, AP and LR dimensions and Hadamard reconstructed along the IS direction with no spectral or spatial filters. The spectra were each automatically frequency aligned and phased in reference to the NAA peak. Relative levels of the i = NAA, Cr, Cho (choline + phosphorylethanolamine), *ml* metabolite in the $j = 1 \dots 224$ VOI voxel of the $k = 1 \dots$ animal were estimated from their peak areas, S_{ijk} , using the SITools-FIT parametric spectral modeling software with Cho, Cr, *ml*, NAA, glutamate and glutamine as full model functions (39). The S_{ijk} -s were scaled into absolute amounts, Q_{ijk} , relative to a 0.5 L sphere of $C_i^{\text{vitro}} = 12.5, 10.0, 3.0$ and 7.5 mM NAA, Cr, Cho and *ml* in water at physiological ionic strength to load the coil and a similar VOI size and position was used in order to sample the \mathbf{B}_1 profile as closely as possible:

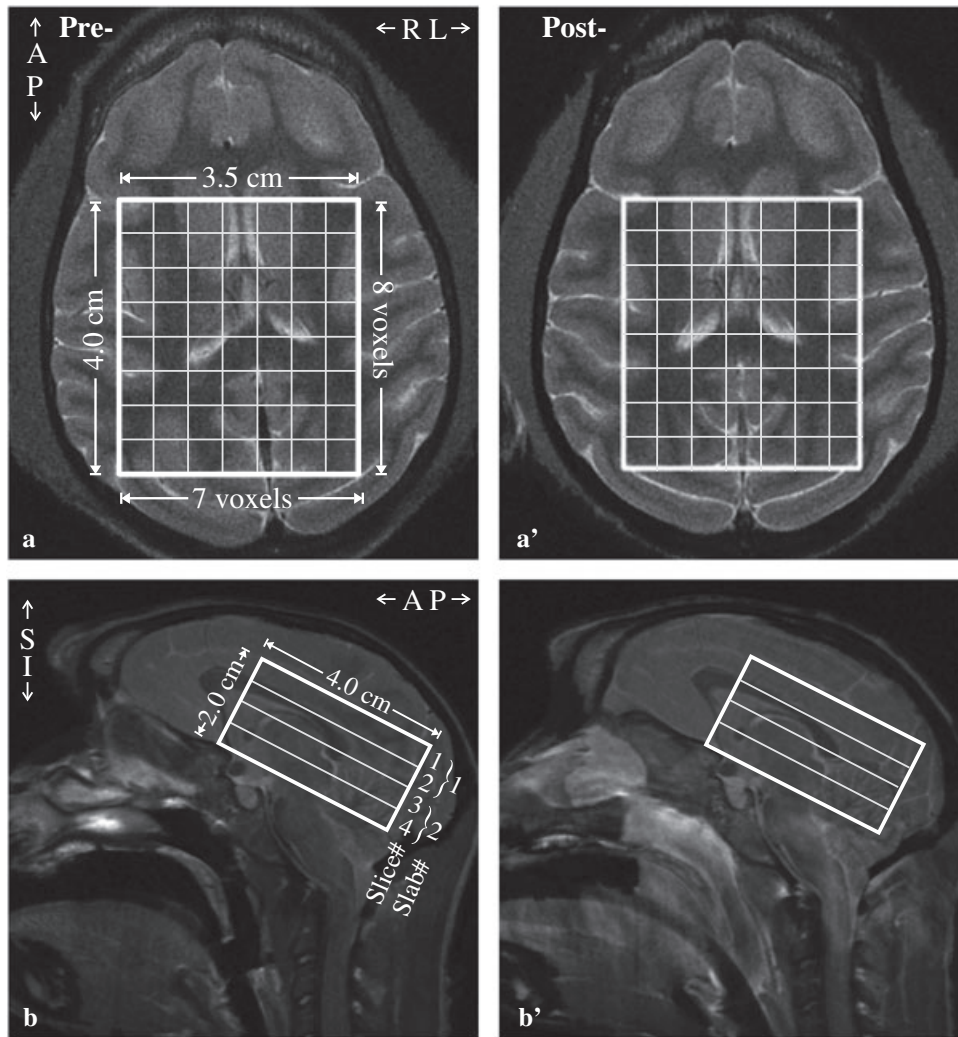


Figure 1. Left (pre-infection): Axial (a) and sagittal (b) T_2 -weighted turbo spin echo (TSE) MRI of a female macaque head showing the location and size of the $4.0 \times 3.5 \times 2.0 \text{ cm}^3$ volume-of-interest (VOI) and localization grid (solid white frame) and two second-order Hadamard slabs, }1 and }2, in the IS direction (b). Right (a', b'): Same as (a, b) 6 weeks post-simian immunodeficiency virus (SIV) infection in that animal. Note similar VOI placement and brain coverage.

$$Q_{ijk} = \frac{C_i^{\text{vitro}}}{V} \cdot \frac{S_{ijk}}{S_{ijR}} \cdot \left(\frac{P_j^{180^\circ}}{P_R^{180^\circ}} \right)^{1/2} \text{ millimoles,} \quad [1]$$

where V is the voxel volume, the S_R is the sphere's voxels' metabolites' signal, $P_j^{180^\circ}$ and $P_R^{180^\circ}$ the RF powers for a non-selective 1 ms 180° inversion pulse on the animal and reference, respectively.

To account for different relaxation times in vivo (T_1^{vivo} , T_2^{vivo}) and in the reference phantom (T_1^{vitro} , T_2^{vitro}), the Q_{ijk} in Equation [1] were corrected with a factor for each metabolite, i :

$$f_i = \frac{\exp(-TE/T_2^{\text{vitro}})}{\exp(-TE/T_2^{\text{vivo}})} \cdot \frac{1 - \exp(-TR/T_1^{\text{vitro}})}{1 - \exp(-TR/T_1^{\text{vivo}})}, \quad [2]$$

with 316, 177 and 264 ms macaque 3 T T_2^{vivo} values for NAA, Cr and Cho used (40) that represent a 60:40 GM:WM tissue fraction-ratio in the VOI. For mI , we used the human $T_2^{\text{vivo}} = 200$ ms value reported by Posse *et al.* (41). We also used the respective macaque 3 T T_1^{vivo} values of 1232, 1238, 1107 and 1170 ms (41,42).

No age-related T_1/T_2 differences were anticipated in this cohort of animals of similar ages as those in a previous report (40,42). The corresponding values measured in the phantom were $T_2^{\text{vitro}} = 483, 288, 200, 233$ ms and $T_1^{\text{vitro}} = 605, 336, 235, 280$ ms.

The global tissue concentration of each metabolite in the VOI, C_{ik} , was obtained as:

$$C_{ik} = \frac{\sum_{j=1}^{224} Q_{ijk}}{\sum_{j=1}^{224} (V_{jk}^{\text{GM}} + V_{jk}^{\text{WM}})} \cdot f_i \text{ mM/g wet weight,} \quad [3]$$

This C_{ik} has the advantage of (number of voxels) $^{1/2} \approx 15$ fold lower variance than the individual voxels' and, hence, is expected to yield proportionally better precision, as described by Kreis (43).

Global GM and WM concentrations

As the CSF does not contribute to the ^1H -MRS signal, the i -th metabolite amount in the j -th voxel in the k -th animal can be modeled as the sum of two compartments' (GM and WM) amounts:

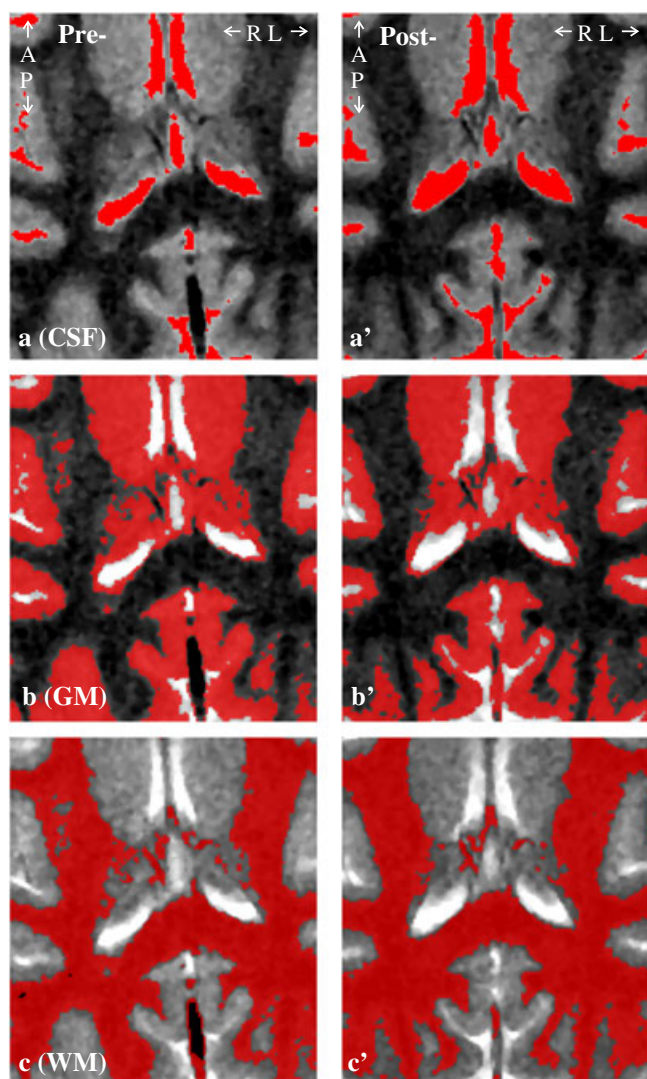


Figure 2. Left: Axial T_2 -weighted turbo spin echo (TSE) image shows the anatomical coverage of the $4.0 \times 3.5 \text{ cm}^2$ volume-of-interest (VOI), overlaid with the: **a:** cerebrospinal fluid (CSF), **b:** gray matter (GM) and **c:** white matter (WM) masks generated by the FireVoxel package. Note the tissue type differentiation performance. Right: **a'-c':** Same as **a-c**, post-infection of the same female macaque.

$$Q_{ijk} = Q_{ijk}^{GM} \cdot f_i^{GM} + Q_{ijk}^{WM} \cdot f_i^{WM} = C_{ik}^{GM} \cdot V_{jk}^{GM} \cdot f_i^{GM} + C_{ik}^{WM} \cdot V_{jk}^{WM} \cdot f_i^{WM}, \quad [4]$$

where C_{ik}^{GM} , C_{ik}^{WM} are the (unknown) global GM and WM metabolites' concentrations and the GM and WM f_i 's are given by Equation [2]. The T_2^{vivo} 's used were 325, 178, 274 and 200 ms for NAA, Cr, Cho and *ml* in GM; 311, 181, 255 and 200 ms in WM (40,41). As no significant GM and WM T_2^{vivo} differences are reported (42), we used the values according to Equation [2]. Although C_{GM}^{WM} and C_{WM}^{GM} cannot both be derived from Equation [4], as the macaque brain's GM and WM spatial heterogeneity is on a scale smaller than the voxels, each has different, independent V_{GM}^{WM} and V_{WM}^{GM} coefficients. The resulting overdetermined system of $j=224$ equations in C_{ik}^{GM} and C_{ik}^{WM} was solved with linear regression. The regression fitting error per voxel was calculated for each metabolite for every animal pre- and post-infection and averaged. The intra-animal coefficient of variation (CV = standard deviation/mean) of this approach was shown to be under 5% for all metabolites (30).

Statistical analyses

The metabolite change for each metabolite and the brain volume change in each compartment (i.e., global VOI tissue, GM and WM) were computed for each animal by taking their pre- minus the post-infection level so that a positive change reflects a decline over time. The lower and upper limits of a 95% confidence interval for the true mean change from the 'pre-' to 'post'-infection scans were estimated for each metabolite in each tissue compartment. The five-animal sample size was insufficient to permit a non-parametric test of whether there was a change in any metabolite for any tissue compartment. As a result, paired-sample *t*-tests were used to assess MRS as well as brain volume changes from the 'pre' to 'post'-infection scans. Significance was tested at the $p < 0.05$ level and SAS version 9.0 (SAS Institute, Cary, NC, USA) was used for all calculations.

RESULTS

An example of the VOI position and size, pre- and post-infection, is shown in Fig. 1. The corresponding GM, WM and CSF VOI masks, segmented from the TSE images for V_{GM} and V_{WM} , are shown in Fig. 2. Spectra from the VOI and metabolic maps generated from them, pre- and post-infection, are shown in Fig. 3. Note that the lateral ventricles in the MRI in Fig. 1a, a' can be detected in the metabolic map for each of the metabolites, reflecting SNR and localization performance. Shimming yielded voxel linewidth of $5.9 \pm 0.9 \text{ Hz}$ FWHM (mean \pm standard deviation) in the 2240 voxels ($224 \text{ voxels/scan} \times 2 \text{ scans/animal} \times 5 \text{ animals}$) and SNRs of NAA: 25 ± 8 , Cr: 16 ± 6 , Cho: 10 ± 3 and *ml*: 10 ± 4 , as shown in Fig. 3. Excellent fit reliability with mean voxel Cramer-Rao lower bounds (CRLBs) below 15% were obtained for NAA, Cr, Cho and *ml*. To optimize the analyses' reliability, VOI voxels were included only if their CRLBs were $< 20\%$ for all metabolites. The global regression fitting errors per voxel for GM/WM were: NAA = 0.04 ± 0.02 , Cr = 0.03 ± 0.01 , Cho = 0.002 ± 0.001 , *ml* = $0.04 \pm 0.04 \text{ mM}$ amongst the five animals and two time points.

GM and WM tissue volumes in the VOI were $16.0 \pm 0.7 \text{ cm}^3$ and $10.1 \pm 0.6 \text{ cm}^3$ pre-infection, and $15.0 \pm 1.1 \text{ cm}^3$ and $10.6 \pm 0.9 \text{ cm}^3$ post-infection. None of these changes were significant ($p > 0.2$ for both). As the % GM and WM volumes changes seem to be offsetting, i.e., the total tissue volume in the VOI appears to remain unchanged, these variations probably reflect different tissue sampling from slight VOI misregistration in the follow-up scan of each animal.

The sums of all 224 spectra in the VOI (equivalent to the numerator of Equation [3]), overlaid with their fits for each animal pre- and post-infection, are shown in Fig. 4. They exhibit SNRs of 390 ± 30 , 223 ± 12 , 151 ± 17 and 144 ± 17 for NAA, Cr, Cho and *ml*, a dramatic $\sim 224^{1/2} \approx 15$ fold gain over the source 0.125 cm^3 voxels (compare Fig. 4 with Fig. 3). The single-voxels' spectral resolution is also maintained in the sums, as reflected by their $8.2 \pm 0.8 \text{ Hz}$ FWHM; a result of pre-alignment, this further contributes to the sums' SNR increase.

The resultant global (Equation [3]) as well as GM and WM (Equation [4]) concentrations for each metabolite in each animal, pre- and post-SIV-infection, are shown in Fig. 5. They reveal a significant global VOI Cho decline (-13% , $p < 0.03$), with a 95% confidence interval (CI) of $[-0.25, -0.08 \text{ mM}]$ and *ml* increase (11% , $p < 0.03$), CI = $[0.18, 1.38 \text{ mM}]$. A significant Cho decline (-20% , $p < 0.003$), CI = $[-0.39, -0.16 \text{ mM}]$ was found only in the GM. Slight increases at the 'trend' level ($p \sim 0.1$) were also

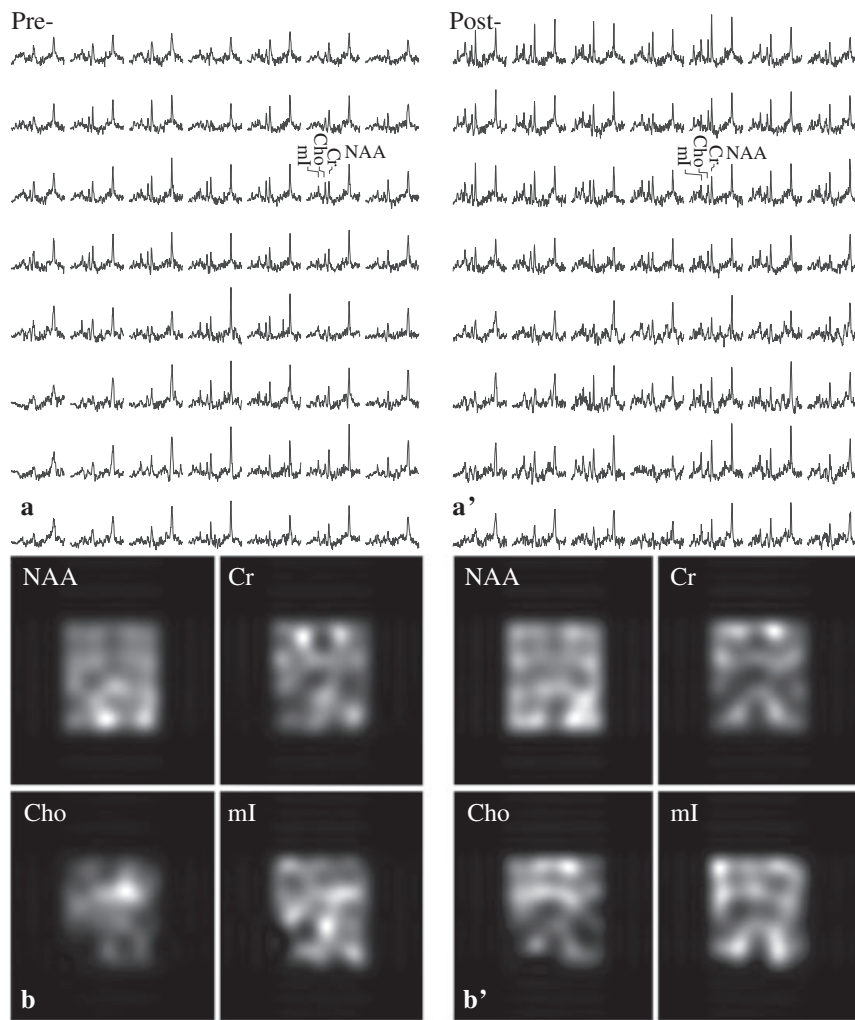


Figure 3. Top: Real part of the 7×8 (LR \times AP) ^1H spectra matrices from the volume-of-interest (VOI) in Fig. 1a and a', on common chemical shift and intensity scales pre- (a) and 6 weeks post- (a') SIV infection. Note the signal-to-noise ratio (SNR) in those $(0.5)^3 = 0.125 \text{ cm}^3$ voxels: *N*-acetylaspartate (NAA): 25 ± 8 , creatine (Cr): 16 ± 6 , choline (Cho): 10 ± 3 and *m*yo-*i*nositol (*mI*): 10 ± 4 and spectral resolution, leading to excellent fit reliability reflected by voxel Cramer–Rao lower bounds (CRLBs) below 15% for these four metabolites. Bottom (b, b'): NAA, Cr, Cho, and *mI* metabolic maps from the spectra in a, a'. Note the gross anatomical features reflecting spatial localization.

observed in the WM Cr and *mI*, perhaps reflecting the small sample size and smaller VOI WM volume (see above; the WM volume was on average two-thirds of the GM's). Since NAA is known to always decline in all adult neuro-pathologies, we tested at the single-sided level and found a significant global decline in the whole VOI (-9% , $p < 0.04$), $\text{CI} = [-1.31, 0.07 \text{ mM}]$ and in the WM (-8% , $p = 0.05$) $\text{CI} = [-1.23, 0.13 \text{ mM}]$, but no significant change in GM. No metabolite differences greater than two standard deviations from the mean of all animals were observed between males and females when the group was divided according to gender.

DISCUSSION

Although several SIV-infected macaque model ^1H -MRS studies have been reported to date, these have been limited by low, $> 3 \text{ cm}^3$ spatial resolution singlevoxels that excluded $>95\%$ of the brain and suffered from CSF, GM and WM partial volumes (21–23). To overcome such limitations, we combined data from high spatial resolution (0.125 cm^3) 3D multi-voxel MRS imaging

with tissue segmentation from the MRI. This enabled us to analyze the metabolic and structural data from hundreds of voxels cooperatively, increasing the overall precision, at the cost of sensitivity to possible regional or specific structure variations (30,43).

Due to the sporadic nature and low incidence of HAND and its consequent paucity of post-mortem studies, non-human primate models are an attractive alternative to histopathology for studying its neuropathogenesis. In this context, ^1H -MRS provides a non-destructive tool for detecting brain metabolite abnormalities in intact animals, facilitating longitudinal studies that histopathology does not. Towards this end, this study aimed to quantify the global GM and WM changes associated with SIV-infection in order to test the hypothesis that global neuro-axonal injury and glial cell activation develop in an accelerated non-human primate model of HAND.

WM neuronal dysfunction

Indeed, we found a significant NAA decline in WM that appears earlier, or is more profound, than in GM. Although evidence of

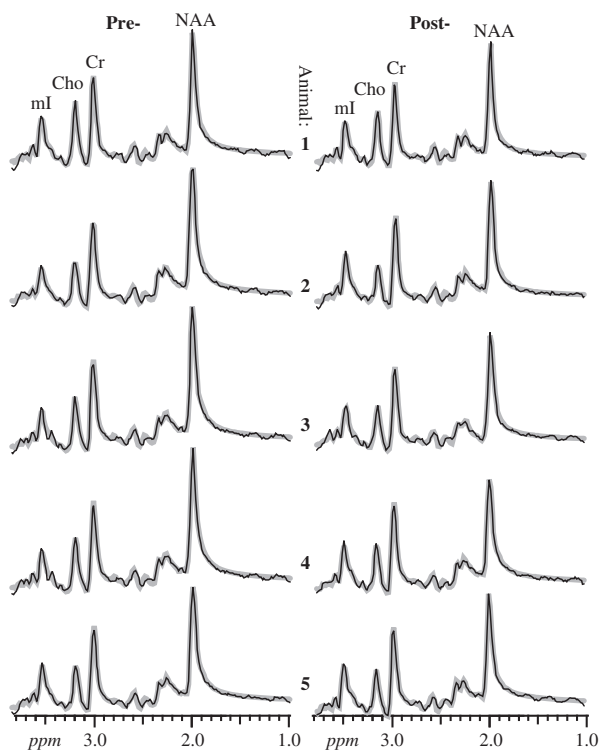


Figure 4. Real part of the aligned and summed ¹H spectra from all volume-of-interest (VOI) voxels (thin black lines) representing Equation [3], for each of the animals pre- (left) and 4 (animals 4 and 5) or 6 (animals 1–3) weeks post-simian immunodeficiency virus (SIV) infection (right), superimposed with their fitted model functions (thick gray lines), on common intensity and chemical shift scales. Animals 1 and 2 are female; 3–5 male. Note the excellent signal-to-noise ratios (SNRs) [reflected by Cramer–Rao lower bounds (CRLBs) of less than 2% for the four metabolites] and spectral resolution compared with individual voxels.

focal neuronal damage in the frontal cortex was seen with single-voxel ¹H-MRS (22), it is possible that global GM dysfunction does not occur until later stages of infection, as suggested previously (27). Nonetheless, a finding of lower WM NAA is consistent with *ex vivo* studies showing NAA/Cr decline in centrum semiovale and frontal WM in acute- and chronically-infected animal and human samples (44). Several previous *in vivo* animal studies also found 5–10% WM NAA/Cr decreases 4 weeks *post*-infection (23,45,46), consistent with us, and some even showed that WM NAA decline 27 days *post*-infection was proportional to synaptic and dendritic deterioration and neuronal loss in quantitative immunohistochemistry (23,46).

Diffuse GM and WM glial activation

Increased global *ml* levels support our hypothesis of diffuse glial activation (28,29,47). Previous HIV studies have also suggested a role for gliosis, reflected by elevated *ml* in both GM and WM of patients with mild HIV-dementia and clinically asymptomatic patients (12,48); these fit well with immunohistochemical studies showing astrocytic and microglial hypertrophy in both the GM and WM of HIV patients with, or without, dementia (49). In SIV-infected macaque models, elevated *ml* has been reported in several GM and WM regions using single voxel ¹H-MRS (22). Evidence seems to suggest a correspondence with increased levels of glial fibrillary acidic protein and ionized calcium binding

adaptor molecule-1, immunohistochemical markers of astrogliosis and microglial activation, respectively, at 4 (or 8) weeks *post*-infection (46).

GM host immune response

The observed 20% global GM Cho decline (see Fig. 5) is consistent with a host immunological response to developing SIV encephalitis, reported previously in the basal ganglia (50). That is, immunopathological evidence has shown that macaques with basal ganglia Cho/Cr near or below uninfected levels at 4 weeks *post*-infection (after an initial increase at 2 weeks *post*-infection) revealed no later signs of encephalitis, whereas those whose levels remained elevated did (50). Moreover, previous studies of both the traditional (21) as well as accelerated (46) SIV macaque models of HAND have also demonstrated large reductions in Cho and Cho/Cr (after initial elevation) 2 to 4 weeks *post*-infection, consistent with our findings of decreased Cho at 4 weeks.

Although it has not been established what role this return to pre-infection levels plays in the context of disease progression, it is reasonable that an immune response is involved given the similar Cho/Cr changes reported after neuroprotective treatment in SIV-infected macaques (22,45), and after antiretroviral treatment in HIV-infected patients (51). Furthermore, both treatments have been shown to support the host immune defense through: (i) downregulation of microglial activation in the former (52); and (ii) a reduction of infected monocyte trafficking into the central nervous system in the latter (23).

Finally, increased energy demand may also occur as a result of glial activation, as reflected by slight increases in WM Cr. A previous study (46) showed that significant Cr elevation at 8-weeks *post*-infection compared with pre-infection corresponded with greater histopathological evidence of gliosis.

Caveats

This study is also subject to several limitations. First, the decision to maximize the sensitivity to diffuse, global changes, especially for the weaker *ml* signal, comes at the cost of localization. Although the original MRS imaging data are available, regional analyses may suffer 10× lower sensitivity to metabolic changes owing to 22–45% intra-voxel CVs (53). Consequently, a 25% decline in parietal cortical neuron number 4 weeks after SIV-infection (46) would go undetected. Second, because of the air-tissue interfaces (i.e. paranasal sinuses) in the frontal head region that cause severe B₀ field inhomogeneity (54), and signal dropout, our VOI placement was limited to exclude most of the frontal brain – an area known to be affected in HAND. However, since our method assesses global GM and WM, exclusion or inclusion of specific region(s) should not significantly impact the findings in diffuse diseases. For example, given their relatively modest, 2.2 cm³, 14% (55) fraction on the VOI's 16 cm³ GM volume and the fact that changes there are on the order of % (see Fig. 3), areas vulnerable to high viral burden, e.g. basal ganglia, cannot in and of themselves explain the global GM changes observed. Third, although we account for T₁ and T₂ in *healthy* macaques, possible pathology effects on either remain unknown. Determining these effects was too costly and time-consuming, especially since pathology-related changes may vary over the 4–6 week infection period. However, the use of short TE = 33 ms and TR ≈ T₁ has been shown to reduce the metabolic quantification variations from T₁ and T₂ variations of up to 10% to below the ~5%

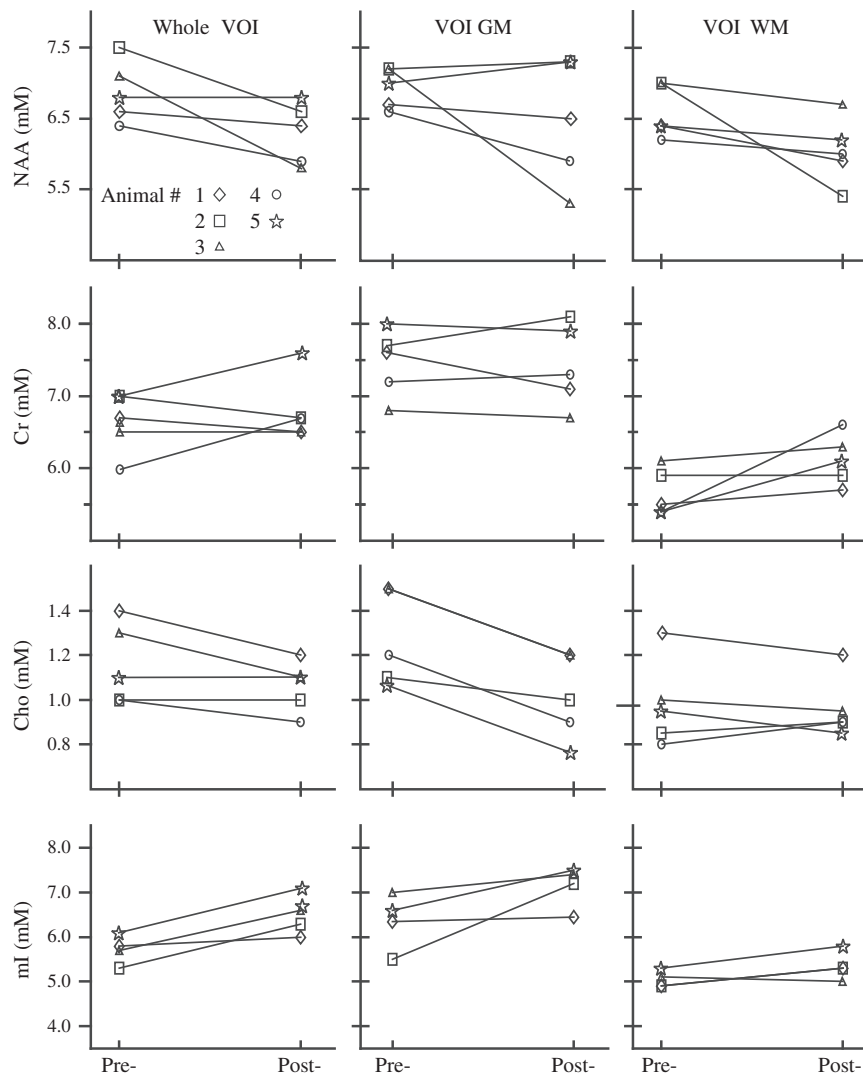


Figure 5. *N*-acetylaspartate (NAA), creatine (Cr), choline (Cho) and *myo*-inositol (*ml*) concentrations' line-plots for all animals, pre- and 4 (animals 4–5) or 6 (animals 1–3) weeks post-simian immunodeficiency virus (SIV) infection, for the whole volume-of-interest (VOI) and its gray (GM) and white matter (WM). Note significant >10% declines in VOI Cho and NAA, elevated *ml*, as well as GM Cho and WM NAA declines.

voxel SNR (42,56). Fourth, because viral and host immune function can vary over a 2-week period (23), the use of two post-infection scan times could have obscured some effects. Due to cost constraints and a lack of preliminary differences between the two groups, we combined their data to improve statistical power. Logistical constraints notwithstanding, future studies would benefit from more animals scanned at multiple times, including closer to infection, when alterations in cerebral metabolism owing to initial viral activity may be more evident.

Our results reveal global tissue injury and recovery while also distinguishing GM- from WM-related dysfunction during the later stages of SIV infection in an accelerated macaque model of HAND. Although host immunological response appears a likely explanation to some of the changes observed during viral infection, its disparate effects in GM and WM suggest distinct pathological pathways that need additional study. These, for example, might examine how neuroprotective intervention in conjunction with anti-inflammatory agents affect the GM and WM and whether either alone, or taken together, might be better strategies for treatment of the disease.

Acknowledgements

We thank Drs Andrew A. Maudsley and Brian J. Soher for their SITools-FITT software and Dr Joanne Morris and Ms Shannon Luboyeski for animal veterinary care. The study was supported by NIH Grants EB01015, NS050520, NS050041, NS051129, NS059331, NS040237 and NS059331. The Athinoula A. Martinos Center for Biomedical Imaging is supported by National Center for Research Resources grant number P41RR14075. Assaf Tal acknowledges support from the Human Frontiers Science Project's Cross-Disciplinary Fellowship.

REFERENCES

1. Cysique LA, Maruff P, Brew BJ. Prevalence and pattern of neuropsychological impairment in human immunodeficiency virus-infected/acquired immunodeficiency syndrome (HIV/AIDS) patients across pre- and post-highly active antiretroviral therapy eras: a combined study of two cohorts. *J. Neurovirol.* 2004; 10: 350–357.

2. Brew BJ, Crowe SM, Landay A, Cysique LA, Guillemin G. Neurodegeneration and ageing in the HAART era. *J. Neuroimmune Pharmacol.* 2009; 4: 163–174.
3. Sacktor N, McDermott MP, Marder K, Schifitto G, Selnes OA, McArthur JC, Stern Y, Albert S, Palumbo D, Kieburz K, De Marcaida JA, Cohen B, Epstein L. HIV-associated cognitive impairment before and after the advent of combination therapy. *J. Neurovirol.* 2002; 8: 136–142.
4. Pialoux G, Fournier S, Moulignier A, Poveda JD, Clavel F, Dupont B. Central nervous system as a sanctuary for HIV-1 infection despite treatment with zidovudine, lamivudine and indinavir. *AIDS* 1997; 11: 1302–1303.
5. Cunningham PH, Smith DG, Satchell C, Cooper DA, Brew B. Evidence for independent development of resistance to HIV-1 reverse transcriptase inhibitors in the cerebrospinal fluid. *AIDS* 2000; 14: 1949–1954.
6. Bhaskaran K, Mussini C, Antinori A, Walker AS, Dorrucci M, Sabin C, Phillips A, Porter K. Changes in the incidence and predictors of human immunodeficiency virus-associated dementia in the era of highly active antiretroviral therapy. *Ann. Neurol.* 2008; 63: 213–221.
7. Kaul M, Garden GA, Lipton SA. Pathways to neuronal injury and apoptosis in HIV-associated dementia. *Nature* 2001; 410: 988–994.
8. Aylward EH, Henderer JD, McArthur JC, Brettschneider PD, Harris GJ, Barta PE, Pearson GD. Reduced basal ganglia volume in HIV-1-associated dementia: results from quantitative neuroimaging. *Neurology* 1993; 43: 2099–2104.
9. Archibald SL, Masliah E, Fennema-Notestine C, Marcotte TD, Ellis RJ, McCutchan JA, Heaton RK, Grant I, Mallory M, Miller A, Jernigan TL. Correlation of in vivo neuroimaging abnormalities with postmortem human immunodeficiency virus encephalitis and dendritic loss. *Arch. Neurol.* 2004; 61: 369–376.
10. Thompson PM, Lee AD, Dutton RA, Geaga JA, Hayashi KM, Eckert MA, Bellugi U, Galaburda AM, Korenberg JR, Mills DL, Toga AW, Reiss AL. Abnormal cortical complexity and thickness profiles mapped in Williams syndrome. *J. Neurosci.* 2005; 25: 4146–4158.
11. Castelo JM, Courtney MG, Melrose RJ, Stern CE. Putamen hypertrophy in nondemented patients with human immunodeficiency virus infection and cognitive compromise. *Arch. Neurol.* 2007; 64: 1275–1280.
12. Chang L, Ernst T, Leonido-Yee M, Walot I, Singer E. Cerebral metabolite abnormalities correlate with clinical severity of HIV-1 cognitive motor complex. *Neurology* 1999; 52: 100–108.
13. Meyerhoff DJ, MacKay S, Bachman L, Poole N, Dillon WP, Weiner MW, Fein G. Reduced brain N-acetylaspartate suggests neuronal loss in cognitively impaired human immunodeficiency virus-seropositive individuals: in vivo ¹H magnetic resonance spectroscopic imaging. *Neurology* 1993; 43: 509–515.
14. Mohamed MA, Lentz MR, Lee V, Halpern EF, Sacktor N, Selnes O, Barker PB, Pomper MG. Factor analysis of proton MR spectroscopic imaging data in HIV infection: metabolite-derived factors help identify infection and dementia. *Radiology* 2010; 254: 577–586.
15. Lentz MR, Kim WK, Lee V, Bazner S, Halpern EF, Venna N, Williams K, Rosenberg ES, Gonzalez RG. Changes in MRS neuronal markers and T cell phenotypes observed during early HIV infection. *Neurology* 2009; 72: 1465–1472.
16. Campsmith ML RP, Hall HI, Green T. *MMWR Weekly*. Volume 2008: Div of HIV/AIDS Prevention, National Center for HIV/AIDS, Viral Hepatitis, STD, and TB Prevention, CDC; 2008.
17. Desrosiers RC. The simian immunodeficiency viruses. *Annu. Rev. Immunol.* 1990; 8: 557–578.
18. Murray EA, Rausch DM, Lendvay J, Sharer LR, Eiden LE. Cognitive and motor impairments associated with SIV infection in rhesus monkeys. *Science* 1992; 255: 1246–1249.
19. Burudi EM, Fox HS. Simian immunodeficiency virus model of HIV-induced central nervous system dysfunction. *Adv. Virus Res.* 2001; 56: 435–468.
20. Zink MC, Amedee AM, Mankowski JL, Craig L, Didier P, Carter DL, Munoz A, Murphey-Corb M, Clements JE. Pathogenesis of SIV encephalitis. Selection and replication of neurovirulent SIV. *Am. J. Pathol.* 1997; 151: 793–803.
21. Greco JB, Westmoreland SV, Ratai EM, Lentz MR, Sakaie K, He J, Sehgal PK, Masliah E, Lackner AA, Gonzalez RG. In vivo ¹H MRS of brain injury and repair during acute SIV infection in the macaque model of neuroAIDS. *Magn. Reson. Med.* 2004; 51: 1108–1114.
22. Ratai EM, Pilkenton SJ, Greco JB, Lentz MR, Bombardier JP, Turk KW, He J, Joo CG, Lee V, Westmoreland S, Halpern E, Lackner AA, Gonzalez RG. In vivo proton magnetic resonance spectroscopy reveals region specific metabolic responses to SIV infection in the macaque brain. *BMC Neurosci.* 2009; 10: 63.
23. Williams K, Westmoreland S, Greco J, Ratai E, Lentz M, Kim WK, Fuller RA, Kim JP, Autissier P, Sehgal PK, Schinazi RF, Bischofberger N, Piatak M, Lifson JD, Masliah E, Gonzalez RG. Magnetic resonance spectroscopy reveals that activated monocytes contribute to neuronal injury in SIV neuroAIDS. *J. Clin. Invest.* 2005; 115: 2534–2545.
24. Gonzalez RG, Cheng LL, Westmoreland SV, Sakaie KE, Becerra LR, Lee PL, Masliah E, Lackner AA. Early brain injury in the SIV-macaque model of AIDS. *AIDS* 2000; 14: 2841–2849.
25. Mankowski JL, Queen SE, Tarwater PM, Fox KJ, Perry VH. Accumulation of beta-amyloid precursor protein in axons correlates with CNS expression of SIV gp41. *J. Neuropathol. Exp. Neurol.* 2002; 61: 85–90.
26. Berman NE, Marcario JK, Yong C, Raghavan R, Raymond LA, Joag SV, Narayan O, Cheney PD. Microglial activation and neurological symptoms in the SIV model of NeuroAIDS: association of MHC-II and MMP-9 expression with behavioral deficits and evoked potential changes. *Neurobiol. Dis.* 1999; 6: 486–498.
27. Xing HQ, Moritoyo T, Mori K, Tadakuma K, Sugimoto C, Ono F, Hayakawa H, Izumo S. Simian immunodeficiency virus encephalitis in the white matter and degeneration of the cerebral cortex occur independently in simian immunodeficiency virus-infected monkey. *J. Neurovirol.* 2003; 9: 508–518.
28. Soares DP, Law M. Magnetic resonance spectroscopy of the brain: review of metabolites and clinical applications. *Clin. Radiol.* 2009; 64: 12–21.
29. Mountford CE, Stanwell P, Lin A, Ramadan S, Ross B. Neurospectroscopy: the past, present and future. *Chem. Rev.* 2010; 110: 3060–3086.
30. Tal A, Kirov I, Gonen O. The Role of Gray and White Matter Segmentation in Quantitative Proton MR Spectroscopic Imaging. *NMR Biomed.* 2012; 25(12): 1392–1400.
31. Williams K, Alvarez X, Lackner AA. Central nervous system perivascular cells are immunoregulatory cells that connect the CNS with the peripheral immune system. *Glia* 2001; 36: 156–164.
32. Williams KC, Hickey WF. Central nervous system damage, monocytes and macrophages, and neurological disorders in AIDS. *Annu. Rev. Neurosci.* 2002; 25: 537–562.
33. Ratai EM, Pilkenton S, He J, Fell R, Bombardier JP, Joo CG, Lentz MR, Kim WK, Burdo TH, Autissier P, Annamalai L, Curran E, O'Neil SP, Westmoreland SV, Williams KC, Masliah E, Gilberto Gonzalez R. CD8 + lymphocyte depletion without SIV infection does not produce metabolic changes or pathological abnormalities in the rhesus macaque brain. *J. Med. Primatol.* 2011; 40: 300–309.
34. Goelman G, Liu S, Hess D, Gonen O. Optimizing the efficiency of high-field multivoxel spectroscopic imaging by multiplexing in space and time. *Magn. Reson. Med.* 2006; 56: 34–40.
35. Goelman G, Liu S, Fleysher R, Fleysher L, Grossman RI, Gonen O. Chemical-shift artifact reduction in Hadamard-encoded MR spectroscopic imaging at high (3T and 7T) magnetic fields. *Magn. Reson. Med.* 2007; 58: 167–173.
36. Mareci T, Brooker H. Essential considerations for spectral localization using indirect gradient encoding of spatial information. *J. Magn. Reson.* 1991; 92: 229–246.
37. Mikheev A, Nevsky G, Govindan S, Grossman R, Rusinek H. Fully automatic segmentation of the brain from T1-weighted MRI using Bridge Burner algorithm. *J. Magn. Reson. Imaging* 2008; 27: 1235–1241.
38. Sled JG, Zijdenbos AP, Evans AC. A nonparametric method for automatic correction of intensity nonuniformity in MRI data. *IEEE Trans. Med. Imag.* 1998; 17: 87–97.
39. Soher BJ, Young K, Govindaraju V, Maudsley AA. Automated spectral analysis III: application to in vivo proton MR spectroscopy and spectroscopic imaging. *Magn. Reson. Med.* 1998; 40: 822–831.
40. Liu S, Gonen O, Fleysher R, Fleysher L, Babb JS, Soher BJ, Joo CG, Ratai EM, Gonzalez RG. Metabolite proton T(2) mapping in the healthy rhesus macaque brain at 3 T. *Magn. Reson. Med.* 2009; 62: 1292–1299.
41. Posse S, Otazo R, Caprihan A, Bustillo J, Chen H, Henry PG, Marjanska M, Gasparovic C, Zuo C, Magnotta V, Mueller B, Mullins P, Renshaw P, Ugurbil K, Lim KO, Alger JR. Proton echo-planar spectroscopic imaging of J-coupled resonances in human brain at 3 and 4 Tesla. *Magn. Reson. Med.* 2007; 58(2): 236–244.
42. Liu S, Fleysher R, Fleysher L, Joo CG, Ratai EM, Gonzalez RG, Gonen O. Brain metabolites B1-corrected proton T1 mapping in the rhesus macaque at 3 T. *Magn. Reson. Med.* 2010; 63: 865–871.

43. Kreis R, Slotboom J, Hofmann L, Boesch C. Integrated data acquisition and processing to determine metabolite contents, relaxation times, and macromolecule baseline in single examinations of individual subjects. *Magn. Reson. Med.* 2005; 54: 761–768.
44. Cheng LL, Ma MJ, Becerra L, Ptak T, Tracey I, Lackner A, Gonzalez RG. Quantitative neuropathology by high resolution magic angle spinning proton magnetic resonance spectroscopy. *Proc. Natl. Acad. Sci. U.S.A.* 1997; 94: 6408–6413.
45. Ratai EM, Bombardier JP, Joo CG, Annamalai L, Burdo TH, Campbell J, Fell R, Hakimelahi R, He J, Autissier P, Lentz MR, Halpern EF, Masliah E, Williams KC, Westmoreland SV, Gonzalez RG. Proton magnetic resonance spectroscopy reveals neuroprotection by oral minocycline in a nonhuman primate model of accelerated NeuroAIDS. *PLoS One* 2010; 5: e10523.
46. Ratai EM, Annamalai L, Burdo T, Joo CG, Bombardier JP, Fell R, Hakimelahi R, He J, Lentz MR, Campbell J, Curran E, Halpern EF, Masliah E, Westmoreland SV, Williams KC, Gonzalez RG. Brain creatine elevation and N-Acetylaspartate reduction indicates neuronal dysfunction in the setting of enhanced glial energy metabolism in a macaque model of neuroAIDS. *Magn. Reson. Med.* 2011; 66: 625–634.
47. Brand A, Richter-Landsberg C, Leibfritz D. Multinuclear NMR studies on the energy metabolism of glial and neuronal cells. *Dev. Neurosci.* 1993; 15: 289–298.
48. Laubenberger J, Haussinger D, Bayer S, Thielemann S, Schneider B, Mundinger A, Hennig J, Langer M. HIV-related metabolic abnormalities in the brain: depiction with proton MR spectroscopy with short echo times. *Radiology* 1996; 199: 805–810.
49. Power C, Kong PA, Crawford TO, Wesselingh S, Glass JD, McArthur JC, Trapp BD. Cerebral white matter changes in acquired immunodeficiency syndrome dementia: alterations of the blood–brain barrier. *Ann. Neurol.* 1993; 34: 339–350.
50. Fuller RA, Westmoreland SV, Ratai E, Greco JB, Kim JP, Lentz MR, He J, Sehgal PK, Masliah E, Halpern E, Lackner AA, Gonzalez RG. A prospective longitudinal in vivo ¹H MR spectroscopy study of the SIV/macaque model of neuroAIDS. *BMC Neurosci.* 2004; 5: 10.
51. Chang L, Ernst T, Leonido-Yee M, Witt M, Speck O, Walot I, Miller EN. Highly active antiretroviral therapy reverses brain metabolite abnormalities in mild HIV dementia. *Neurology* 1999; 53: 782–789.
52. Zemke D, Majid A. The potential of minocycline for neuroprotection in human neurologic disease. *Clin. Neuropharmacol.* 2004; 27: 293–298.
53. Wu WE, Kirov, II, Zhang K, Babb JS, Joo CG, Ratai EM, Gonzalez RG, Gonen O. Cross-sectional and longitudinal reproducibility of rhesus macaque brain metabolites: A proton MR spectroscopy study at 3 T. *Magn. Reson. Med.* 2011; 65(6): 1522–1531.
54. Duyn JH, Gillen J, Sobering G, van Zijl PC, Moonen CT. Multisection proton MR spectroscopic imaging of the brain. *Radiology* 1993; 188: 277–282.
55. Yin D, Valles FE, Fiandaca MS, Forsayeth J, Larson P, Starr P, Bankiewicz KS. Striatal volume differences between non-human and human primates. *J. Neurosci. Methods* 2009; 176: 200–205.
56. Zaaraoui W, Fleysher L, Fleysher R, Liu S, Soher BJ, Gonen O. Human brain-structure resolved T(2) relaxation times of proton metabolites at 3 Tesla. *Magn. Reson. Med.* 2007; 57: 983–989.